AIAA SciTech Forum
6-10 January 2020, Orlando, FL
AIAA Scitech 2020 Forum

10.2514/6.2020-0362

Spectral Analysis of a Hypersonic Boundary Layer on a Right, Circular Cone

A. Hameed* N. J. Parziale†

Stevens Institute of Technology, Hoboken, NJ 07030, USA

L. Paquin‡ C. Butler§ S. J. Laurence¶

University of Maryland, College Park, MD 20742, USA

Results from a stability investigation using quad-focused laser differential interferometry (q-FLDI) and high-speed schlieren cinematography of hypersonic flow over a cooled and uncooled 5° half-angle cone are presented in this paper. The frequency and phase-speed of the largest-amplitude disturbance (largest N factor) as predicted by STABL and measured by FLDI or schlieren were in excellent agreement for the room-temperature cases and good agreement for the cooled-wall cases. A comparison between a cooled-wall and room-temperature shot at nominally the same Reynolds number shows the interesting result of the later transition to turbulence for the cooled-wall shot. Our hypothesis is: cooled-wall cases have higher growth rates and higher most-amplified frequencies. Because there is less wind-tunnel noise at higher frequency, transition will occur at a higher Reynolds number.

P	= Pressure, (MPa)
T	= Temperature, (K)
ρ	= Density, (kg/m^3)
M	= Mach number, (-)
Re^{Unit}	= Unit Reynolds number, (1/m)
Re^{M}	= Reynolds number at measurement location, (-)
State	= State of boundary layer, (-)
N_{factor}	= N factor, (-)
s_M	= Measurement location along cone, (mm)
δ	= Boundary layer thickness at measurement location, (mm)
U	= Streamwise velocity, (m/s)
u_{conv}	= Convective velocity, (m/s)
$U_E/(2\delta)$	= Normalized frequency scale, (kHz)
f^M	= Measured second-mode frequency, (kHz)
f^S	= Predicted second-mode frequency, (kHz)

Subscript

R	= Reservoir
x	= Free stream
E	= Edge condition at measurement location
W	= Cone wall

*Graduate Student, Mechanical Engineering, Castle Point on Hudson, Hoboken, New Jersey, 07030. Student AIAA Member.
†Assistant Professor, Mechanical Engineering, Castle Point on Hudson, Hoboken, New Jersey, 07030. Senior AIAA Member.
‡Graduate Student, Aerospace Engineering, Department of Aerospace Engineering, College Park, Maryland, 20742. Student AIAA Member.
§Graduate Student, Aerospace Engineering, Department of Aerospace Engineering, College Park, Maryland, 20742. Student AIAA Member.
¶Associate Professor, Aerospace Engineering, Department of Aerospace Engineering, College Park, Maryland, 20742. Senior AIAA Member.

I. Introduction

The transition from laminar to turbulent flow in supersonic and hypersonic boundary layers has been a topic of interest for over 50 years.[1] Research on the subject has been multi-disciplinary and has involved public, private, and governmental institutions. Accurate prediction of the transition location is useful in estimating the heat transferred to hypersonic vehicles, resulting in optimizations of the vehicle's thermal protective systems.

In hypersonic flows at zero angle of attack, a major mechanism of transition to turbulence is receptivity to freestream disturbances leading to modal growth.[2] Within these hypersonic boundary layers, the first mode coexists with the trapped second and higher modes.[3] At the higher Mach numbers of the hypersonic regime, the first mode can be completely stabilized but the inviscid second mode becomes the dominant instability wave.[4,5] The second-mode instability has been detected using hot-wire anemometry, pressure transducers, and heat-flux gauges for measurements at the surface. In contrast, optical methods such as schlieren cinematography[6–9] and focused laser differential interferometry (FLDI) provide off-surface measurements of the second mode instability within the boundary layer.

In this paper, we compare FLDI and schlieren experimental results to STABL calculations concerning hypersonic flow over a right-circular cone at zero angle of attack with varying wall-temperature ratio. Specifically, spectral content and phase-speed measurement are discussed for several different cases.

II. Focused Laser Differential Interferometry

A focused laser differential interferometer (FLDI) is a common-path polarization interferometer[10,11] pioneered by Smeets and George in the mid-1970s. Smeets and George demonstrated the use of FLDI for measurements of a density profile within a shock front, unsteady boundary layers, and, amongst other things, developed an eight beam pair FLDI set-up to examine the flow field around a blunt cone.[12] More recently, Parziale[13–19] used the FLDI technique to characterize boundary layer transition in the Caltech T5 reflected-shock tunnel.[20] Jewell et al.[21,22] used two-point FLDI to make correlation measurements in boundary layers and turbulent jets. Weisberger et al.[23] used FLDI to make measurements in the NASA Langley 20-Inch Mach 6 wind tunnel and observed second-mode wave packets. Ceruzzi and Cadou quantified the capabilities of a two-point FLDI set-up and measured the density gradient fluctuations and mean velocities in a round turbulent air jet.[24] Additionally, other researchers are using FLDI and variants to explore a myriad of flows.[25–27]

A basic FLDI setup is developed by first expanding a linearly polarized laser beam using a diverging lens. The expanding beam is then circularly polarized by a quarter-wave plate before being split into two beams of mutually orthogonal, linear polarization by a Wollaston prism. The diverging beams are collimated by locating the Wollaston prism at the focal point (or close to) of a converging lens. The converging lens brings the beams to a focus. The setup is symmetric about the focus; the beams are recombined by a second Wollaston prism and polarizer, and their interference signal is measured by a change in intensity on a photodetector.[28]

The FLDI is sensitive to the phase difference between the beam pairs of the instrument. The phase difference between a beam pair is due to the separate optical path lengths traversed by the individual beams in the FLDI setup as a result of differing indices of refraction. Unwanted signals are rejected by the FLDI outside of the focus area by filtering due to finite beam separation, finite beam width, and beam overlap.

This basic FLDI setup can be expanded by the addition of polarizers and Wollaston prisms upstream of the focus to generate additional beam pairs, and corresponding photodetectors downstream of the focus to measure their interference. In this work, a four beam pair, q-FLDI setup was utilized to characterize the instability within the boundary layer. The components of the q-FLDI setup are shown in Fig. 1.

Fig. 2 shows q-FLDI beam profiles at varying positions away from the beam focus. At the focus, the beam pairs occupy distinct volumes in space, with a measurable separation distance between them. The overlap between the beam pairs increases with increasing distance from the focus. For the setup shown in Fig. 2, at 15 mm away from the focus, there is almost complete overlap between each of the beam pairs.

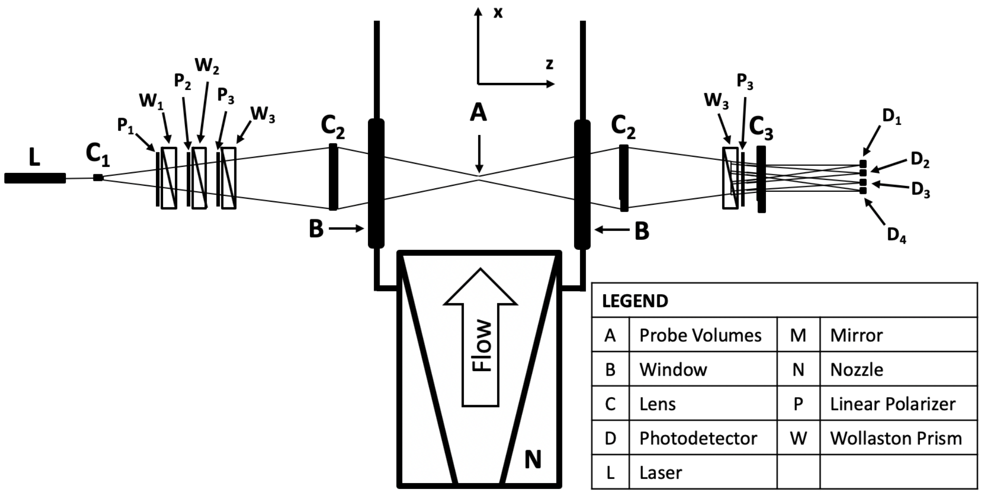

Figure 1: Components of a q-FLDI setup. For clarity, the four beam pairs and eight probe volumes generated by the setup are omitted.

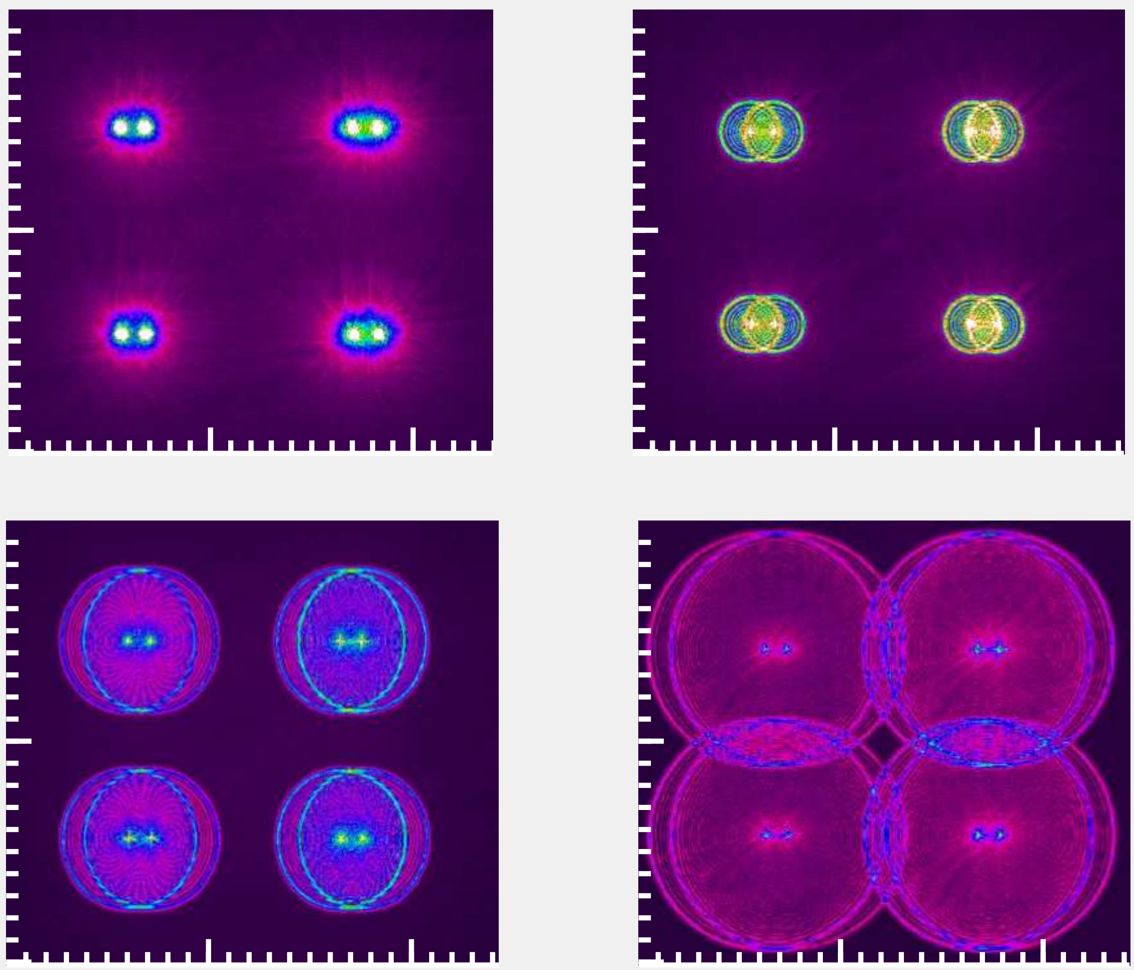

(c) (d)

Figure 2: q-FLDI beam profiles at (a) focus, (b) 5 mm upstream of focus, (c) 10 mm upstream of focus, (d) 15 mm upstream of focus. Major tick marks are at 1 mm and minor tick marks are at 0.1 mm.

A single frequency, 532 nm, Cobolt 05-01 laser was used, which was operated at its maximum power output of 1500 mW. An alternating array of three Thorlabs WPQ20ME-532 quarter-wave plates and three custom-made United Crystals 3-inch Wollaston prisms stacked in lens tubes attached to a rotation mount was used to orthogonally polarize, split, and orient the beam pairs. A 150 mm focal length converging lens focused the four beam pairs at the center of HyperTERP's 14-inch wide test section, immediately above the test article.

The beam inter- and intraspacing (depicted in Fig. 3) is a function of the Wollaston prism's position along the beam propagation axis and its separation angle. Wollaston prisms W_1 and W_2 generate the desired beam interspacing, while the beam instraspacing is determined by W_3. For shots 2 to 7, the Wollaston prism beam separation angles were $W_1 = 30$ arcminutes, $W_2 = 20$ arcminutes, $W_3 = 2$ arcminutes. For shots 10, 18, and 20, the beam instraspacing was decreased by using a Wollaston prism of a smaller separation angle, $W_3 = 0.5$ arcminutes. Using these components, the beam inter- and intraspacing shown in Fig. 4 was achieved for the two Wollaston prism arrangements.

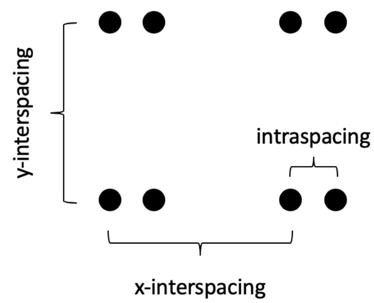

Figure 3: Depiction of beam inter- and intraspacing in a four beam pair q-FLDI setup.

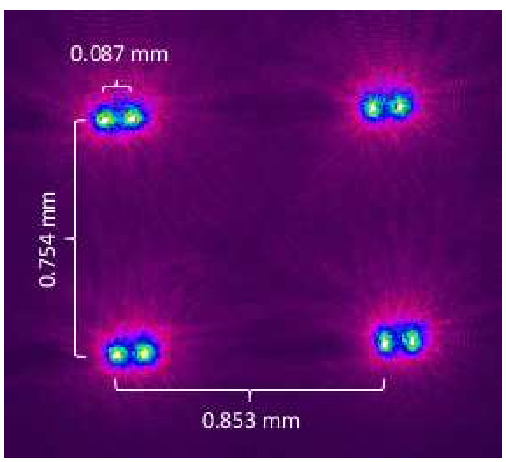

(a)

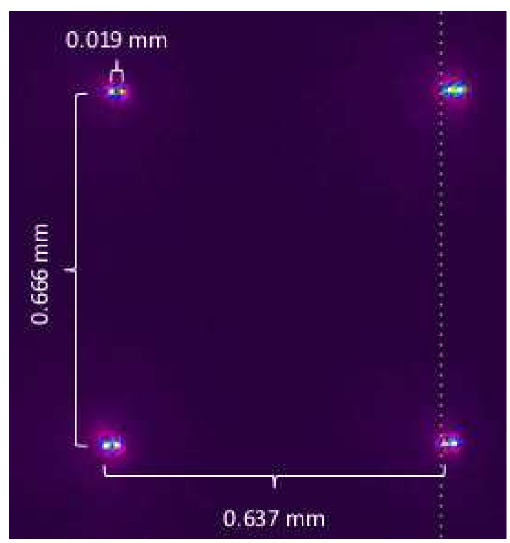

(b)

Figure 4: Picture of the four beam pairs generated using the (a) 30-20-2 arcminute Wollaston prism arrangement and the (b) 30-20-0.5 arcminute Wollaston prism arrangement. Due to their close proximity, the camera's aperture was greatly reduced to capture the 8 distinct beams in (b).

Only the intraspaced beam pairs were recombined downstream of the focus using the corresponding Wollaston prism, thus producing four interfering beams. These four beams were spread relative to each other, allowing each of them to be focused on individual Thorlabs DET36A2 photodetectors. The signal from the four photodetectors was collected using two linked Cleverscope CS328A Oscilloscopes.

The wall-normal position of the beams was carefully adjusted by changing the height of the upstream converging lens, C_2. A measurement of the wall-normal position was gained by raising a razor blade loosely attached to the tip of a dial indicator zeroed at the cone surface. The wall-normal position was recorded once the razor blade passed through the middle of the lower and upper pairs of beams. For these experiments, the lower set of beams was located approximately 0.2-0.3 mm above the cone surface and the upper set of beams was located approximately 0.9-1.0 mm above the cone surface.

III. Stability Analysis

PSE-Chem is a part of the STABL software package described in Johnson et al.,[29] Johnson,[30] and Wagnild.[31] First, PSE-Chem analyzes the mean flow over the cone computed by DPLR for a perfect gas, as warranted by the moderate temperatures in the flow. Second, the method of normal modes is applied to the perfect-gas Navier-Stokes equations, where it is assumed that the boundary layer is quasi-parallel and the disturbances have the form

$$q'(s,z,t) = \hat{q}(y)\exp(i(\alpha s + \beta z - \omega t)), \tag{1}$$

where q' is a disturbance at a position along the generator of the cone s, azimuthal position z, and time t. The amplitude of the disturbance is considered to be only a function of the wall-normal distance, $\hat{q} = \hat{q}(y)$. The streamwise wave number is α, the azimuthal wave number is β, and the angular frequency is ω. The spatial linear stability problem is analyzed where the frequency (ω) is real and the wavenumbers are complex ($\alpha = \alpha_r + \alpha_i$); non-zero azimuthal wavenumbers (β) are not considered in this analysis, as disturbance is assumed to be two-dimensional. The phase speed is $c_r^S = \omega/\alpha_r$. The linear stability calculation results are then used as initial values for the parabolized stability equation (PSE) analysis, which is used to account for the non-parallel nature of the boundary layer. The procedure for the PSE analysis is found in Johnson.[30] The amplification factor (N) is then computed as

$$N = \int_{s_U}^{s_D} \sigma ds, \tag{2a}$$

$$\sigma = -Im(\alpha) + \frac{1}{2E}\frac{dE}{ds}, \tag{2b}$$

$$E = \int_{\Omega} \overline{\rho}\left(|\hat{u}|^2 + |\hat{v}|^2 + |\hat{w}|^2\right) dV, \tag{2c}$$

Linear-stability diagrams are presented in Figs. 5a and 5c for Shots 10 and 18, respectively. We choose to present these two calculations because they correspond to a room-temperature (Shot 10) and cooled-wall case (Shot 18) at the same edge Reynolds number based on measurement location. In Figs. 5a and 5c, we place a black bar at the FLDI or schlieren measurement location and we present this slice in frequency space as Figs. 5b and 5d. Here, we present the growth rate and phase speed as calculated by STABL. Consistent with Mack[3] and many other researchers, it can be seen that wall cooling increases the growth rate and most-amplified frequency, the latter being due to the decreased boundary-layer thickness. The conditions for the corresponding experiments are found in Table 1 and the comparison of the STABL calculations and the experimental results are summarized in Table 2.

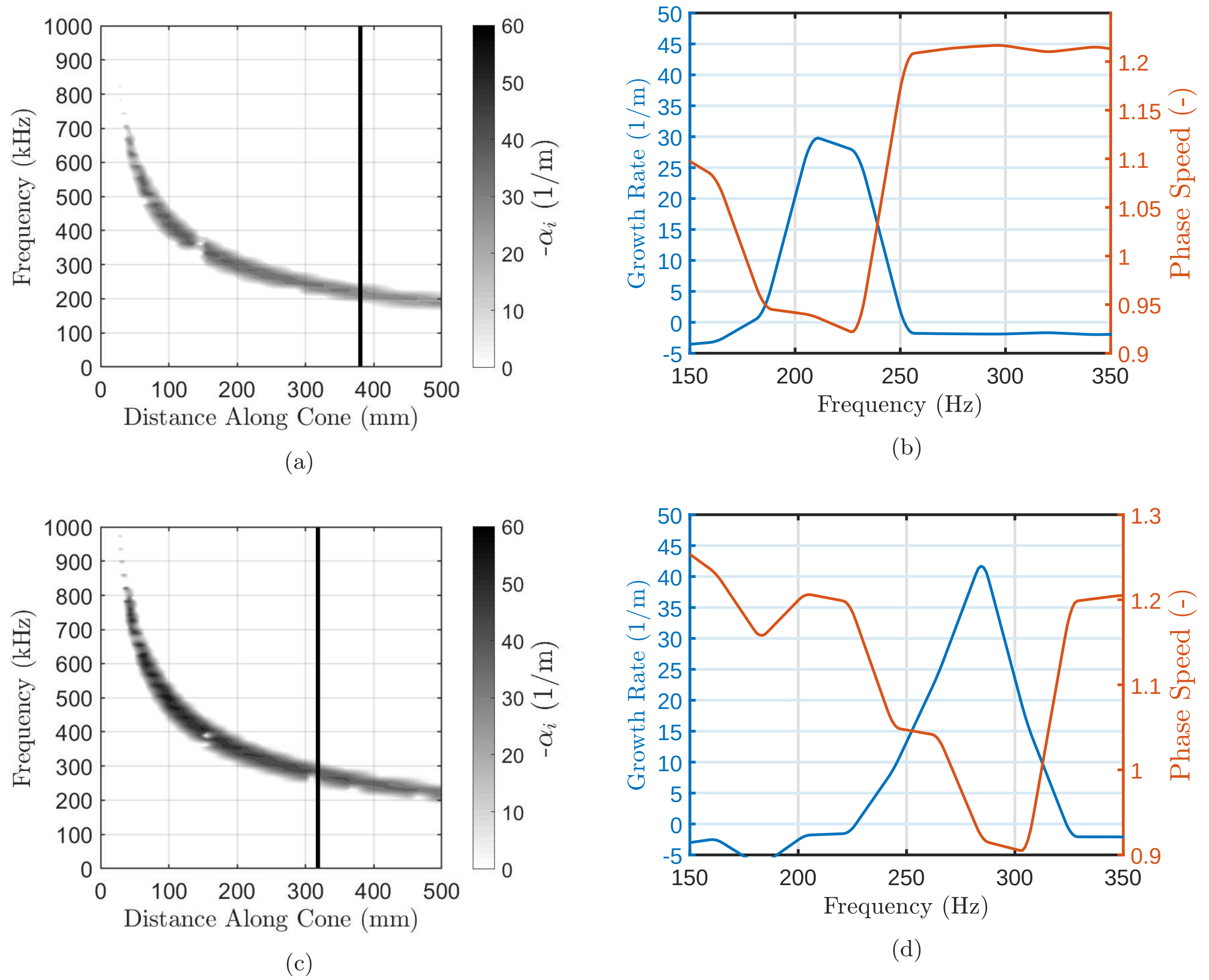

Figure 5: (a) and (b): Shot 10 - room-temperature cone - Re_E^M=2.20e6, $T_W/T_E = 2.9$. (c) and (d): Shot 18 - cooled-wall cone - Re_E^M=2.25e6, $T_W/T_E = 2.2$. (a) and (c): Linear-stability diagrams. Black line corresponds to measurement location. (b) and (d): growth rate and phase speed at the measurement location denoted by the black line.

IV. Facility and Experimental Setup

All experiments were performed in the hypersonic shock tunnel, HyperTERP, operated by the University of Maryland. A schematic of the facility is shown in Fig. 6, with major components labeled. The unheated driver section is 3 m long and the driven section is 10 m long; both have an internal diameter of 100 mm. They are separated by the primary diaphragm station. A double-burst mechanism incorporating two mylar diaphragms is employed to allow accurate control of the burst conditions. The driven section is isolated from the nozzle and downstream components by a secondary mylar diaphragm, just upstream of the nozzle throat. For the experiments performed in this work, a contoured nozzle with an exit diameter of 220 mm and a design Mach number of 6.0 was manufactured and installed. The nozzle exhausts into a cylindrical test section with an internal diameter of 300 mm.

The tunnel is typically run under tailored conditions to maximize test time. For the shots performed in this work, the driver gas was a mixture of helium to achieve various enthalpies. A typical reservoir pressure trace is shown in Fig. 7; we see that the pressure remains approximately constant for 6 ms. This is shorter than the theoretically predicted test time, a discrepancy that we attribute to deviations from ideal burst in the double-diaphragm mechanism.

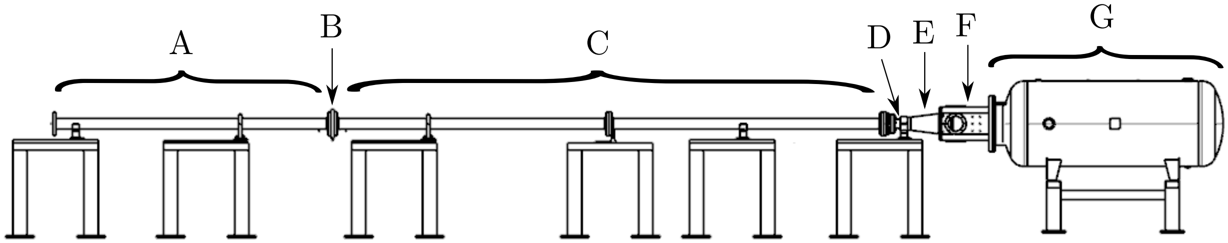

Figure 6: Schematic of the shock tunnel facility employed in the experimental component of this study: (A) driver section; (B) primary (double) diaphragm; (C) driven section; (D) secondary diaphragm; (E) Mach-6 nozzle; (F) test section; (G) dump tank.

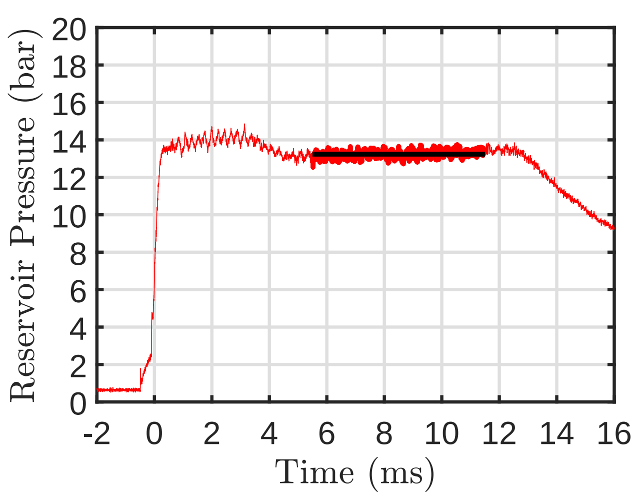

Figure 7: Typical stagnation pressure trace in HyperTERP for this experimental investigation. This is taken from Shot 7. The black line denotes the test time.

The corresponding flow conditions for each of the shots performed in this work are presented in Table 1. The reservoir conditions were determined using the measured shock speed and Cantera[32] with the Shock and Detonation Toolbox.[33] To calculate the nozzle exit conditions, a simulation was performed using DPLR with the calculated reservoir conditions. The results of the DPLR simulation were used to perform a stability analysis using STABL, providing the boundary-layer edge conditions.

Table 1: Shot conditions. P_R, T_R, U_x, T_x, ρ_x, M_x, Re_x^{Unit}, U_E, T_E, ρ_E, M_E, Re_E^{Unit}, and T_W, are the reservoir pressure, reservoir temperature, exit velocity, exit temperature, exit density, exit Mach number, exit unit Reynolds number, edge velocity, edge temperature, edge density, edge Mach number, edge unit Reynolds number, and wall temperatuer, respectively.

Shot	P_R	T_R	U_x	T_x	ρ_x	M_x	Re_x^{Unit}	U_E	T_E	ρ_E	M_E	Re_E^{Unit}	T_W
	(MPa)	(K)	(m/s)	(K)	(kg/m^3)	(-)	(1/m)	(m/s)	(K)	(kg/m^3)	(-)	(1/m)	(K)
2	1.37	785	1187	89	0.026	6.27	5.06e6	1176	102	0.037	5.80	6.06e6	300
3	1.05	802	1199	91	0.020	6.25	3.75e6	1188	105	0.028	5.78	4.49e6	300
4	0.76	782	1183	89	0.015	6.23	2.85e6	1172	103	0.021	5.76	3.40e6	300
5	1.64	795	1196	90	0.031	6.28	5.90e6	1185	103	0.043	5.81	7.07e6	300
6	2.03	825	1219	93	0.036	6.29	6.85e6	1208	107	0.051	5.82	8.22e6	300
7	1.32	796	1195	90	0.025	6.26	4.78e6	1184	104	0.035	5.79	5.71e6	300
10	1.35	798	1197	90	0.025	6.27	4.83e6	1186	104	0.035	5.80	5.79e6	300
18	1.62	788	1190	89	0.031	6.28	5.91e6	1179	102	0.043	5.81	7.10e6	221
20	1.93	792	1194	89	0.036	6.29	6.96e6	1183	103	0.050	5.82	8.36e6	226
21	1.58	888	1265	101	0.026	6.27	4.79e6	1253	116	0.037	5.80	5.77e6	226
22	1.95	805	1204	91	0.036	6.29	6.88e6	1193	104	0.050	5.82	8.25e6	215

Instability measurements for Shots 2-7, 10, 18 and 20 were made using the FLDI technique, while schlieren high-speed cinematography was used to perform similar measurements for shots 21 and 22. The cone's wall was cooled for shots 18, 20, 21, and 22.

The test article for these experiments was a slender, 5° half-angle cone with a nominally sharp nosetip, mounted at zero incidence. For the cooled-wall experiments, the cone was cooled through thermal contact with the immersion probe of the PolyScience IP-100 cooler. This cooler operated by circulating refrigerant within its metallic probe and typically maintained a probe temperature around -95 C. The aluminum frustum of the cone was machined in two halves with a groove along the center axis between them. The cooler probe, 16 mm in diameter, was inserted into the groove through the base of the cone, and thermal paste was applied to increase the amount of thermal contact. A thermocouple measured the temperature of the cone surface 5.2 cm upstream of the base. This system effectively cooled the cone at a rate of about -3C/min for the first 13 minutes, but the level of cooling decayed over time due to thermal contact between the cone, sting, and test section walls. Typically, the temperature of the cone would asymptote around -60 C if the cooler remained operational for 1.5 hours.

V. Results and Discussion

In this section, we discuss the measurement of disturbances in a hypersonic boundary layer using schlieren and FLDI for nominally similar cases where the wall is and is not actively cooled. Key parameters from both the measurements and the STABL computations are summarized in Table 2. We should note that STABL does a good job of predicting the frequency of the boundary-layer instability for most cases. In the cases of the cooled-wall, (Shots 18, 20, 21, 22), STABL slightly under-predicts the frequency content. Further research is required to understand this discrepancy, including a more thorough characterization of the cone surface temperature distribution under cooling. STABL also appears to accurately predict the second mode phase speed.

In Fig. 8, we present two FLDI results, Shot 10 where second-mode instability was observed throughout the test time, and Shot 6, where turbulent broadband response was observed throughout test time. The spectrogram presented in Fig. 8 (top) shows evidence of this observation. In Fig. 8 (middle), we zoom in to

200 µs of test time where we observe second-mode wave packets and broadband response as measured by two FLDI detectors separated by a small distance (Fig. 4). Fig. 8 (bottom) shows the correlation of these signals in time, and with accurate measurement of the FLDI beams displacement, we can get the convective time. Importantly, for beam spacings this small, it is the phase velocity (not group velocity) that is measured by correlation.

In Fig. 9, we present an averaged PSD of the FLDI response for the four FLDI detectors again for two experiments: a laminar case with second-mode waves and a turbulent case. The four detectors in Fig. 4 nominally show the same response in each case. FLDI detectors 1-2 and 3-4 are located at the same wall-normal location.

In Fig. 10a, we show one of the FLDI detector's responses with increasing Reynolds number. One can see the magnitude of the instability grow, with eventual broadband turbulent response. We note the moderate Reynolds number difference (a factor of 2-3) between incipient instability and transition to turbulence.

To compare the FLDI and schlieren technique spectral responses, we compare results at nominally the same condition in Fig. 10b. The spectra appear to match very well bringing confidence in both measurement techniques. We note that the lower noise floor of the FLDI measurement allows both first and second harmonics to be discerned, whereas only the first harmonic is weakly visible in the schlieren signal.

We compare a cooled and room-temperature case in Fig. 11a at nominally the same Reynolds number. The results for the cooled case (Shot 18) show appreciably higher frequency content than that for the experiment carried out when the cone was at room temperature (Shot 10).

An additional cooled/room-temperature comparison is presented in Fig. 11b, where we show two shots with the FLDI technique at nominally the same Reynolds number. Conventional wisdom (of these authors) would suggest that, in general, the room temperature cases would transition to turbulence at higher Reynolds numbers than cooled-wall cases because the growth rates of the second-mode instability are typically higher for a cooled wall. This is not borne out in the two experiments shown in Fig. 11b. A hypothesis for this counter-intuitive result is: for the cooled-wall cases, even though the growth rates are higher, the most-amplified frequencies that lead to transition are also higher. At higher frequencies, however, the intensity of the free-stream disturbances that ultimately excite the second-mode instability within the boundary layer is lower, potentially leading to delayed transition. This observation is consistent with the N factor calculations in Table 2. Moreover, researchers have found that the N factor of transition is correlated to disturbance frequency.[34, 35]

Table 2: Comparison of FLDI, schlieren, and STABL results. M_E, Re_E^{Unit}, s_M, Re_E^M , State, N_{factor}, δ, $U_E/(2\delta)$, f^M, f^S, T_W/T_E, u_{conv}, $c^M = u_{conv}^M/U_E$, and c_r^S are the edge Mach number, the unit Reynolds number, the measurement location, the edge Reynolds number at the point of measurement, the state of the boundary layer (Laminar (L), Instabilities (I), or Turbulent (T)), N factor as calculated by STABL at the measurement location, boundary-layer thickness as calculated by DPLR, normalized frequency scale, measured second-mode frequency, predicted second-mode frequency by STABL, wall-edge temperature ratio, measured phase speed and normalized measure phase speed, phase speed predicted by STABL, respectively.

Shot	M_E	Re_E^{Unit}	s_M	Re_E^M	State	N_{factor}	δ	$U_E/(2\delta)$	f^M	f^S	T_W/T_E	u_{conv}	$c^M = u_{conv}/U_E$	c_r^S
	(-)	(1/m)	(mm)	(-)	(-)	(-)	(mm)	(kHz)	(kHz)	(kHz)	(-)	(m/s)	(-)	(-)
2	5.80	6.06e6	380	2.30e6	T	4.1	2.1	283.6	B	244.1	2.9	1066	0.91	0.92
3	5.78	4.49e6	380	1.71e6	I	2.9	2.4	250.2	240	203.1	2.9	1122	0.94	0.95
4	5.76	3.40e6	380	1.29e6	L	2.6	2.7	215.5	-	182.6	2.9	-	-	0.92
5	5.81	7.07e6	380	2.69e6	T	4.7	1.9	305.7	B	261.3	2.9	1040	0.88	0.92
6	5.82	8.22e6	380	3.12e6	T	5.1	1.8	345.1	B	285.0	2.8	1093	0.90	0.91
7	5.79	5.71e6	380	2.17e6	I	4.0	2.1	280.7	235	237.8	2.9	1120	0.95	0.92
10	5.80	5.79e6	380	2.20e6	I	4.0	2.1	281.1	245	237.8	2.9	1053	0.89	0.92
18	5.81	7.10e6	318	2.25e6	I	5.0	1.6	361.8	320	284.9	2.2	965	0.82	0.91
20	5.82	8.36e6	318	2.65e6	I	5.6	1.5	394.4	350	305.5	2.2	965	0.82	0.91
21	5.80	5.77e6	318	1.83e6	I	4.3	1.7	359.8	300	284.9	2.0	1114	0.89	0.90
22	5.82	8.25e6	318	2.62e6	I	5.7	1.5	404.3	355	308.4	2.1	1124	0.94	0.91

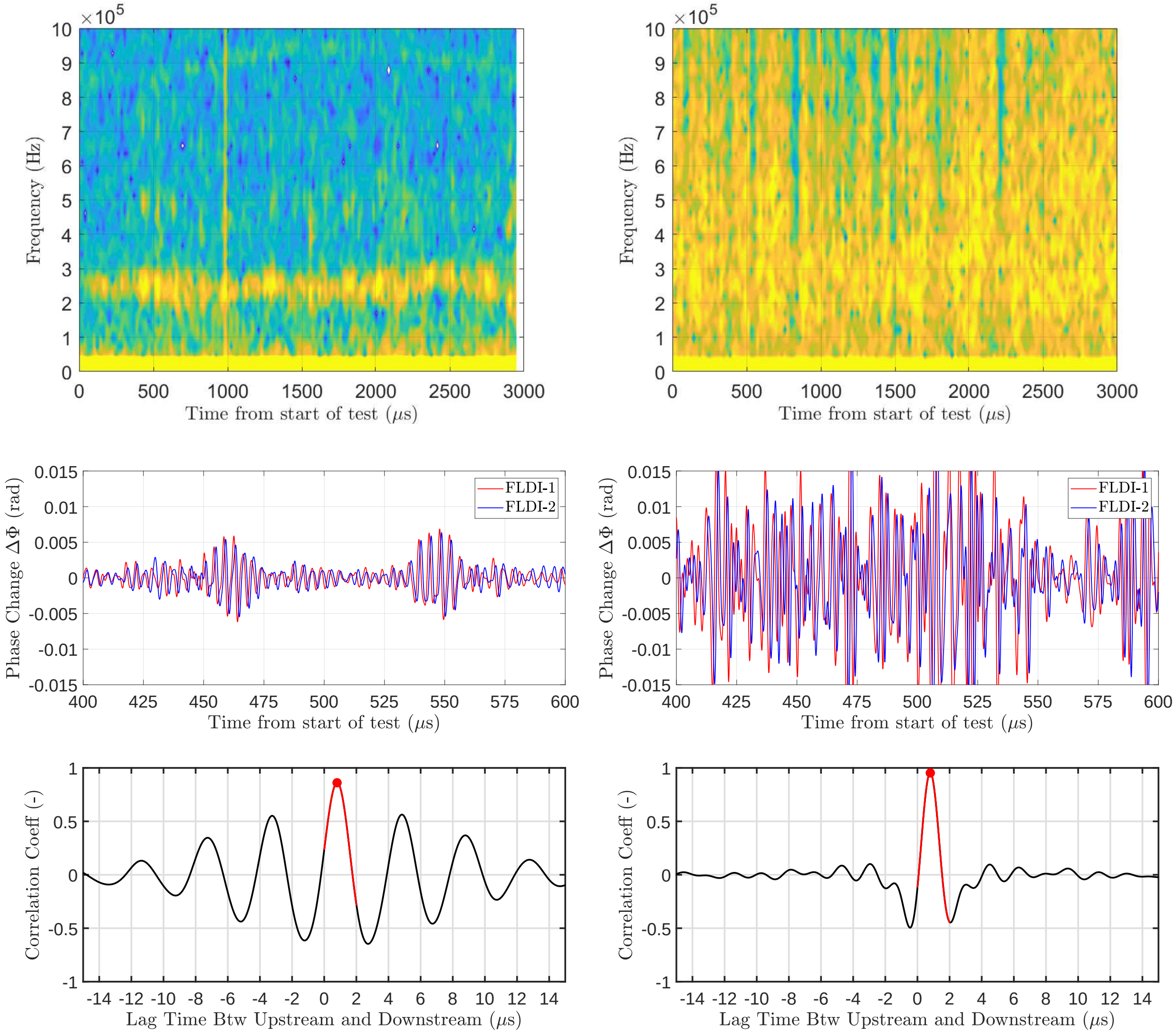

(a) (b)

Figure 8: (a): Shot 10 - Re_E^M=2.20e6 was an experiment where the second mode was observed, (b): Shot 6 - Re_E^M=3.12e6 shows broadband turbulent response. Top shows spectrograms of run time. Middle shows phase change of FLDI for detectors 1 and 2 separated by a short distance (see Fig 4) for short times. Bottom shows the correlation between the FLDI detectors 1 and 2. These lags are used to determine the convective velocity. Red indicates the maximum of a fitted polynomial to the lag data.

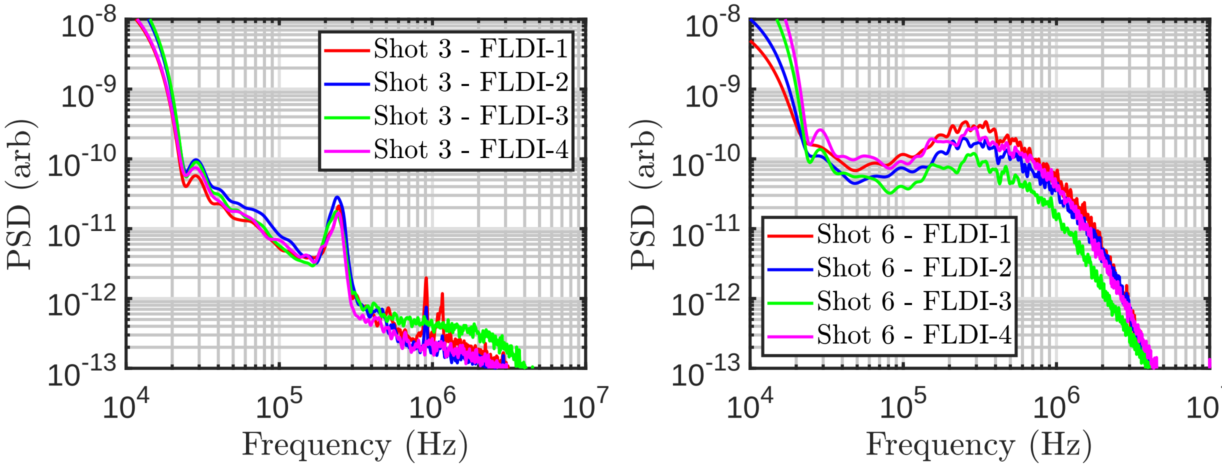

(a) (b)

Figure 9: (a): Shot 3 - Re_E^M=1.71e6 shows a case where the second mode is observed, (b): Shot 6 - Re_E^M=3.12e6 shows broadband turbulent response. Note that in both Shot 3 and Shot 6 (unstable and turbulent) all four FLDI detector responses are similar.

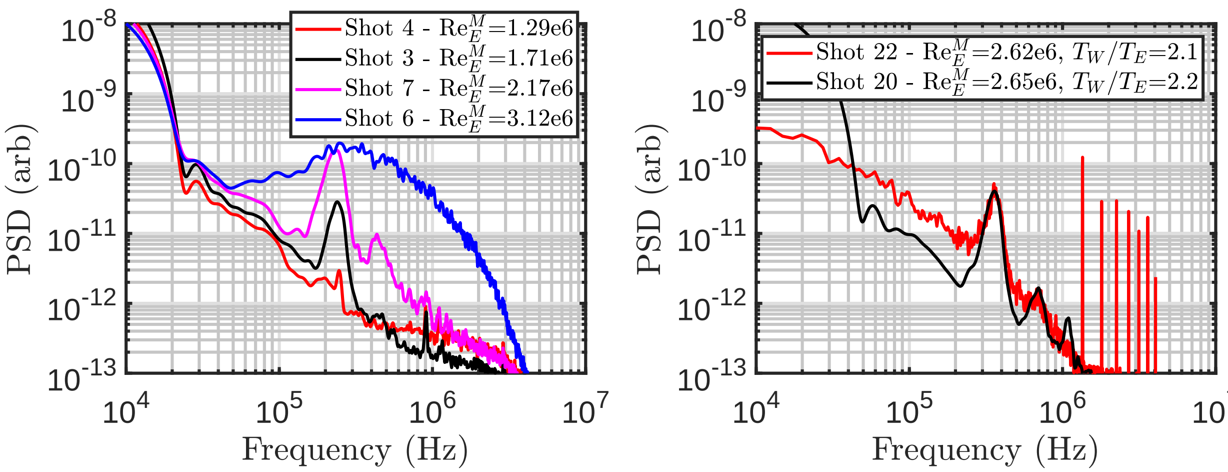

(a) (b)

Figure 10: (a): Shots 4,3,7, and 6 showing the increased second mode amplitude and broadband response and the Reynolds number at the measurement location (Re_E^M) is increased with a fixed wall-temperature ratio (T_W/T_E). (b): At the same Reynolds number and wall-temperature ratio, the schlieren response (Shot 22) and the FLDI response (Shot 20) show excellent agreement in terms of observed second-mode frequency.

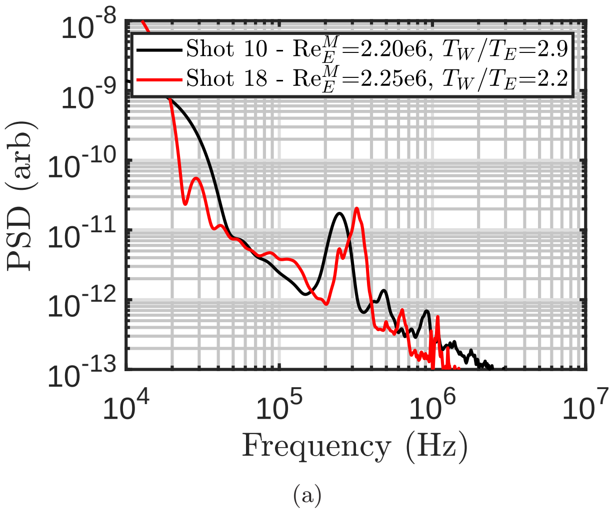

Figure 11: (a): Shots 10 (FLDI) and 18 (FLDI) show that at the same Reynolds number, the observed second-mode frequency is higher for the cooled-wall case (Shot 18) relative to the room-temperature case (Shot 10). (b): For approximately the same Reynolds number, the cool-wall case (Shot 20) shows second-mode boundary-layer instability, while the room-temperature case (Shot 5) show broadband turbulent response.

VI. Conclusions

In this paper, we compare the FLDI and schlieren experimental results to STABL calculations concerning hypersonic flow over a right-circular cone at zero angle of attack with varying wall-temperature ratio. Specifically, spectral content and phase-speed measurement are discussed for several different cases. We found excellent agreement between the FLDI and schlieren experimental methods in terms of resolving the spectral content and phase speed of boundary-layer disturbances. Sensibly, for the cooled-wall cases, the observed second-mode boundary-layer instability had higher frequency content. The frequency and phase-speed of the largest-amplitude disturbance (largest N factor) as predicted by STABL and measured by FLDI or schlieren were also in excellent agreement for the room-temperature cases and good agreement for the cooled-wall cases.

Finally, we observed that the room-temperature wall case transitioned to turbulence at the same Reynolds number where the cooled-wall case remained unstable. Conventional wisdom might suggest that the higher growth rates associated with the cooled-wall cases would result in early transition, relative to the lower growth rates for the room-temperature cases. A hypothesis for this counter-intuitive result is: for the cooled-wall cases, even though the growth rates are higher, the frequency that drives the boundary layer unstable is also higher. At higher frequencies, there is less wind-tunnel noise, thus the boundary layer transitions at a higher Reynolds number.

Acknowledgments

Support for this work was provided by the Air Force Office of Scientific Research Grants FA9550-16-1-0262 and FA9550-18-1-0403; Ivett Leyva of AFOSR is the Program Manager for both grants. Additionally, there was support from Air Force Small Business Innovation Research contracts FA9101-17-P-0094 and FA2487-19-C-0013.

References

[1]Leyva, I. A., "The relentless pursuit of hypersonic flight," *Physics Today*, Vol. 70, No. 11, 2017, pp. 30–36. doi: 10.1063/PT.3.3762.

[2]Fedorov, A., "Transition and Stability of High-Speed Boundary Layers," *Annual Review of Fluid Mechanics*, Vol. 43, 2011,

pp. 79–95. doi: 10.1146/annurev-fluid-122109-160750.

[3]Mack, L. M., "Boundary-Layer Linear Stability Theory," *AGARD Report 709*, Special Course on Stability Transitional Laminar Flows 1984.

[4]Knisely, C. P. and Zhong, X., "Sound radiation by supersonic unstable modes in hypersonic blunt cone boundary layers. I. Linear stability theory," *Physics of Fluids*, Vol. 31, No. 2, 2019, pp. 024103. doi: 10.1063/1.5055761.

[5]Knisely, C. P. and Zhong, X., "Sound radiation by supersonic unstable modes in hypersonic blunt cone boundary layers. II. Direct numerical simulation," *Physics of Fluids*, Vol. 31, No. 2, 2019, pp. 024104. doi: 10.1063/1.5077007.

[6]Laurence, S. J., Wagner, A., Hannemann, K., Wartemann, V., Lüdeke, H., Tanno, H., and Itoh, K., "Time-Resolved Visualization of Instability Waves in a Hypersonic Boundary Layer," *AIAA Journal*, Vol. 50, No. 6, 2012, pp. 243–246. doi: 10.2514/1.56987.

[7]Laurence, S. J., Wagner, A., Ozawa, H., Schramm, J. M., and Hannemann, K., "Visualization of a hypersonic boundary-layer transition on a slender cone," *19th AIAA International Space Planes and Hypersonic Systems and Technologies Conference*, AIAA-2014-3110, Atlanta, Georgia, 2014.

[8]Laurence, S., Wagner, A., and Hannemann, K., "Schlieren-based techniques for investigating instability development and transition in a hypersonic boundary layer," *Experiments in Fluids*, Vol. 55, No. 8, 2014. doi: 10.1007/s00348-014-1782-9.

[9]Kennedy, R. E., Laurence, S. J., Smith, M. S., and Marineau, E. C., "Investigation of the second-mode instability at Mach 14 using calibrated schlieren," *Journal of Fluid Mechanics*, Vol. 845, 2018. doi: 10.1017/jfm.2018.269.

[10]Settles, G. S. and Fulghum, M. R., "The Focusing Laser Differential Interferometer, an Instrument for Localized Turbulence Measurements in Refractive Flows," *Journal of Fluids Engineering*, Vol. 138, No. 10, 2016, pp. 101402. doi: 10.1115/1.4033960.

[11]Danehy, P. M., Weisberger, J., Johansen, C., Reese, D., Fahringer, T., Parziale, N. J., Dedic, C., Estevadeordal, J., and Cruden, B. A., "Non-Intrusive Measurement Techniques for Flow Characterization of Hypersonic Wind Tunnels," *Flow Characterization and Modeling of Hypersonic Wind Tunnels (NATO Science and Technology Organization Lecture Series STO-AVT 325)*, NF1676L-31725 - Von Karman Institute, Brussels, Belgium, 2018.

[12]Smeets, G. and George, A., "Gas Dynamic Investigations in a Shock Tube using a Highly Sensitive Interferometer," Translation of isl internal report 14/71, Original 1971, Translation 1996.

[13]Parziale, N. J., Shepherd, J. E., and Hornung, H. G., "Reflected Shock Tunnel Noise Measurement by Focused Differential Interferometry," *Proceedings of 42nd AIAA Fluid Dynamics Conference and Exhibit*, AIAA-2012-3261, New Orleans, Louisiana, 25-28 June 2012. doi: 10.2514/6.2012-3261.

[14]Parziale, N. J., Jewell, J. S., Shepherd, J. E., and Hornung, H. G., "Optical Detection of Transitional Phenomena on Slender Bodies in Hypervelocity Flow," *Proceedings of RTO Specialists Meeting AVT-200/RSM-030 on Hypersonic Laminar-Turbulent Transition*, NATO, San Diego, California, 16-19 April 2012.

[15]Parziale, N. J., Shepherd, J. E., and Hornung, H. G., "Differential Interferometric Measurement of Instability at Two Points in a Hypervelocity Boundary Layer," *Proceedings of 51st AIAA Aerospace Sciences Meeting Including the New Horizons Forum and Aerospace Exposition*, AIAA-2013-0521, Grapevine, Texas, 7-10 January 2013. doi: 10.2514/6.2013-521.

[16]Parziale, N. J., Shepherd, J. E., and Hornung, H. G., "Differential Interferometric Measurement of Instability in a Hypervelocity Boundary Layer," *AIAA Journal*, Vol. 51, No. 3, 2013, pp. 750–754. doi: 10.2514/1.J052013.

[17]Parziale, N. J., *Slender-Body Hypervelocity Boundary-Layer Instability*, Ph.D. thesis, California Institute of Technology, 2013.

[18]Parziale, N. J., Shepherd, J. E., and Hornung, H. G., "Free-stream density perturbations in a reflected-shock tunnel," *Experiments in Fluids*, Vol. 55, No. 2, 2014, pp. 1665. doi: 10.1007/s00348-014-1665-0.

[19]Parziale, N. J., Shepherd, J. E., and Hornung, H. G., "Observations of hypervelocity boundary-layer instability," *Journal of Fluid Mechanics*, Vol. 781, 2015, pp. 87–112. doi: 10.1017/jfm.2015.489.

[20]Fulghum, M. R., *Turbulence measurements in high-speed wind tunnels using focusing laser differential interferometry*, Ph.D. thesis, The Pennsylvania State University, 2014.

[21]Jewell, J. S., Parziale, N. J., Lam, K.-L., Hagen, B. J., and Kimmel, R. L., "Disturbance and Phase Speed Measurements for Shock Tubes and Hypersonic Boundary-Layer Instability," *Proceedings of 32nd AIAA Aerodynamic Measurement Technology and Ground Testing Conference*, AIAA-2016-3112, Washington, D. C., 13-17 June 2016. doi: 10.2514/6.2016-3112.

[22]Jewell, J. S., Hameed, A., Parziale, N. J., and Gogineni, S. P., "Disturbance Speed Measurements in a Circular Jet via Double Focused Laser Differential Interferometry," *Proceedings of AIAA Scitech 2019*, AIAA-2019-2293, San Diego, California, 7-11 January 2019. doi: 10.2514/6.2019-2293.

[23]Weisberger, J. M., Bathel, B. F., Herring, G. C., King, R. A., Chou, A., and Jones, S. B., "Focused Laser Differential Interferometry Measurements at NASA Langley 20-Inch Mach 6," *Proceedings of AIAA Aviation Forum*, AIAA-2019-2903, Dallas, Texas, 2019. doi: 10.2514/6.2019-2903.

[24]Ceruzzi, A. P. and Cadou, C. P., "Simultaneous Velocity and Density Gradient Measurements using Two-Point Focused Laser Differential Interferometry," *Proceedings of AIAA Scitech 2019*, AIAA-2019-2295, San Diego, California, 7-11 January 2019. doi: 10.2514/6.2019-2295.

[25]Lawson, J. M., Neet, M. C., Grossman, I. J., and Austin, J. M., "Characterization of a Focused Laser Differential Interferometer," *Proceedings of AIAA Scitech 2019*, AIAA-2019-2296, San Diego, California, 7-11 January 2019. doi: 10.2514/6.2019-2296.

[26]Houpt, A. W. and Leonov, S. B., "Focused and Cylindrical-Focused Laser Differential Interferometer Characterization of SBR-50 at Mach 2," *Proceedings of AIAA Aviation 2019*, AIAA-2019-3383, Dallas, Texas, 17-21 June 2019. doi: 10.2514/6.2019-3383.

[27]Vogel, E. A., Coder, J. G., Chynoweth, B. C., and Schneider, S. P., "Experimental and Computational Results of a Cone-Slice-Ramp Geometry at Mach 6," *Proceedings of AIAA Aviation 2019*, AIAA-2019-3593, Dallas, Texas, 17-21 June 2019. doi: 10.2514/6.2019-3593.

[28]Schmidt, B. E. and Shepherd, J. E., "Analysis of focused laser differential interferometry," *Applied Optics*, Vol. 54, No. 28, 2015, pp. 8459–8472. doi: 10.1364/AO.54.008459.

[29]Johnson, H. B., Seipp, T. G., and Candler, G. V., "Numerical Study of Hypersonic Reacting Boundary Layer Transition on Cones," *Physics of Fluids*, Vol. 10, No. 13, 1998, pp. 2676–2685. doi: 10.1063/1.869781.

[30]Johnson, H. B., *Thermochemical Interactions in Hypersonic Boundary Layer Stabity*, Ph.D. thesis, University of Minnesota, Minneapolis , Minnesota, 2000.

[31]Wagnild, R. M., *High Enthalpy Effects on Two Boundary Layer Disturbances in Supersonic and Hypersonic Flow*, Ph.D. thesis, University of Minnesota, Minnesota, 2012.

[32]Goodwin, D. G., "An Open-Source, Extensible Software Suite for CVD Process Simulation," *Proceedings of CVD XVI and EuroCVD Fourteen, M Allendorf, F Maury, and F Teyssandier (Eds.)*, 2003, pp. 155–162.

[33]Browne, S., Ziegler, J., and Shepherd, J. E., "Numerical Solution Methods for Shock and Detonation Jump Conditions," GALCIT - FM2006-006, 2006.

[34]Jewell, J. S., *Boundary-layer transition on a slender cone in hypervelocity flow with real gas effects*, Ph.D. thesis, California Institute of Technology, 2014.

[35]Jewell, J. S., Parziale, N. J., Leyva, I. A., and Shepherd, J. E., "Effects of Shock-Tube Cleanliness on Hypersonic Boundary Layer Transition at High Enthalpy," *AIAA Journal*, Vol. 55, No. 1, 2017, pp. 332–338. doi: 10.2514/1.J054897.